

## Intelligent smartphone-based multimode imaging otoscope for the mobile diagnosis of otitis media: supplement

THIAGO C. CAVALCANTI,<sup>1</sup>  HAH MIN LEW,<sup>1</sup>  KYUNGSU LEE,<sup>1</sup>  
SANG-YEON LEE,<sup>2</sup> MOO KYUN PARK,<sup>2,3,4</sup> AND JAE YOUN  
HWANG<sup>1,3,5</sup>

<sup>1</sup>*Department of Information and Communication Engineering, Daegu Gyeongbuk Institute of Science and Technology, Daegu, Republic of Korea*

<sup>2</sup>*Department of Otorhinolaryngology-Head and Neck Surgery, Seoul National University Hospital, Seoul, Republic of Korea*

<sup>3</sup>*co-corresponding authors*

<sup>4</sup>*aseptic@snu.ac.kr*

<sup>5</sup>*jyhwang@dgist.ac.kr*

---

This supplement published with Optica Publishing Group on 23 November 2021 by The Authors under the terms of the [Creative Commons Attribution 4.0 License](https://creativecommons.org/licenses/by/4.0/) in the format provided by the authors and unedited. Further distribution of this work must maintain attribution to the author(s) and the published article's title, journal citation, and DOI.

Supplement DOI: <https://doi.org/10.6084/m9.figshare.16989346>

Parent Article DOI: <https://doi.org/10.1364/BOE.441590>

## Important Notice to Authors

Attached is a PDF proof of your forthcoming article in Optical Materials Express. The article Manuscript ID is 434715. *No further processing of your paper will occur until we receive your response to this proof.*

**Note:** *Excessive proof corrections submitted by the author can result in significant delays to publication. Please include only essential changes that might be needed to address any shortcomings noticed in the proof-preparation process.*

### Author Queries


Please answer these queries by marking the required corrections at the appropriate point in the text or referring to the relevant line number in your PDF proof.

Q1	The funding information for this article has been generated using the information you provided to OSA at the time of article submission. Please check it carefully. If any information needs to be corrected or added, please provide the full name of the funding organization/institution as provided in the Crossref Open Funder Registry ( <a href="https://search.crossref.org/funding">https://search.crossref.org/funding</a> ).
----	---

### Other Items to Check

- Please note that the original manuscript has been converted to XML prior to the creation of the PDF proof, as described above. The PDF proof was generated using LaTeX for typesetting. The placement of your figures and tables may not be identical to your original paper.
- Please carefully check all key elements of the paper, particularly the equations and tabular data.
- Author list: Please make sure all authors are presented, in the appropriate order, and that all names are spelled correctly.
- If you need to supply new or replacement figures, please upload each figure as an individual PDF file at the desired final figure size. The figure must fit inside the margins of the manuscript, i.e., width no more than 5.3 inches (or 13.46 cm). Confirm the quality of the figures and upload the revised files when submitting proof corrections.

# Determination of optical constants and scattering properties of transparent polymers for use in optoelectronics

JOACHIM BAUER,<sup>1,\*</sup> OKSANA FURSENKO,<sup>2</sup> FRIEDHELM HEINRICH,<sup>1</sup>  
MARKO GUTKE,<sup>1</sup> ECKHART KORNEJEV,<sup>1</sup> OLIVER BROEDEL,<sup>1</sup>  
BIRGIT DIETZEL,<sup>1</sup> ALEXANDER KALTENBACH,<sup>3</sup> MARTIN  
BURKHARDT,<sup>3</sup> MATTHIAS EDLING,<sup>4</sup> PATRICK STEGLICH,<sup>1,2</sup>   
MICHAEL HERZOG,<sup>1</sup> AND SIGURD SCHRADER<sup>1</sup>

<sup>1</sup>Technical University of Applied Sciences Wildau, Hochschulring 1, 15745 Wildau, Germany

<sup>2</sup>IHP – Leibniz-Institut für innovative Mikroelektronik, Im Technologiepark 25, 15236 Frankfurt (Oder), Germany

<sup>3</sup>resintec GmbH, Hellsternstr. 1, 04895 Falkenberg/Elster, Germany

<sup>4</sup>EPIGAP Optronik GmbH, Koepenicker Str. 325, Hs. 40, 12555 Berlin, Germany

\*jobauer@th-wildau.de

**Abstract:** Knowledge of optical constants, i.e. refractive index  $n$  and extinction coefficient  $k$ , and light scattering properties of optical polymers are required to optimize micro-optics for light-emitting diodes in terms of efficiency, color properties and light distribution. We present here a model-based diagnostic approach to determine the optical properties of polymers, which should be particularly useful in the development of plastics for optical applications. Optical constants and scattering coefficients were obtained from transmission and reflection measurements in a wavelength range from UV to NIR taking into account scattering effects due to rough surfaces and volume inhomogeneity. Based on the models for the dielectric function, the molecular optical transition energies  $E_g$ , critical point energies, Urbach energies and exciton transition energies were determined. Rayleigh and Mie scattering model and van de Hulst's anomalous diffraction theory were applied to characterize scattering due to volume inhomogeneities. Scalar diffraction theory was applied to account for surface roughness scattering. Atomic force microscopy with nanomechanical characterization was used to characterize domains in size and shape and to assign optical scattering to a suitable morphological model. The combined optical and mechanical characterization help to improve the qualification of new polymer materials for optical applications.

© 2021 Optical Society of America under the terms of the [OSA Open Access Publishing Agreement](#)

## 1. Introduction

The development of optical functional polymers has allowed high-tech products to be made available for optical processes [1–2,3]. The current requirements and market volume of polymers for optoelectronic applications, such as micro-optics for light-emitting diodes (LEDs) and miniaturized CMOS image sensors [4–7], waveguides [8–15] and optical fibers [16], have led to an increasing demand for cost-effective and high-performance materials and a significant growth in production capacities.

Besides long-term thermal and mechanical stability, optical constants play a key role in the selection of suitable polymers. In this scenario the refractive index  $n$  to account for color dispersion and index matching and a high transmittance are essential for optical functionality.

The extinction coefficient  $k$  is related to absorption and defines the applicability, regarding specific wavelengths. Absorption is an inelastic process that not only attenuates the transmitted light but can also lead to overheating and material degradation, causing serious problems

especially in high power applications such as optical coatings for laser applications or high-power LEDs. In contrast, scattering essentially involves elastic processes with negligible internal energy transfer. Although it is undesirable in many applications, such as imaging optics and light guiding systems, and causes similar light losses to absorption in terms of propagation direction, scattering effects can be used to gain advantage in other applications, such as lighting systems where homogeneous illumination is required. Therefore, a clear distinction between absorption and scattering is required for appropriate material development.

Direct determination of scattering is usually performed by angle-resolved measurements with goniometers or, alternatively, using integrating spheres. The aim of this work is to find a way to distinguish absorption from scattering by combining relatively simple optical setups with a suitable modeling procedure. For the optical measurements we used a commercial double-beam spectrophotometer in transmission, reflection and a home-built interferometric setup in reflection. In this way, the refractive index, the absorption and scattering coefficients could be derived simultaneously from the experimental data by a fitting procedure based on parametric modeling (Section 3.2), which provided a reasonable and sufficient approximation to the experimental data for our purposes.

The optical measurements were supported by nanomechanical characterization using atomic force microscopy (AFM), which in addition to the optical data provide important information on the size of the scattering centers, needed for a model verification. Fourier transform infrared (FTIR) measurements and matrix-assisted laser desorption ionization time-of-flight (Maldi-TOF) mass spectroscopy served as companion methods to provide further insight into the structure of the scattering regions and to substantiate the AFM data.

To experimentally demonstrate the applicability of the proposed method, we used our newly developed polyurethane (PU) based materials, which are particularly suitable for use in optical devices [3]. Due to the ability of urethane groups to form hydrogen bonds, they tend to form molecular aggregates (macro domains) and nano domains which may be analyzed by small-angle X-ray scattering, AFM, IR spectroscopic methods, optical scattering as well as transmission electron microscopy (TEM) [17–31].

In order to clearly separate losses due to absorption and scattering, the optical data were compared with simulated ones obtained by different methods within the framework of a best-fit procedure. The scattering due to surface roughness is calculated based on scalar diffraction theory according to Helmholtz-Kirchhoff [32–34].

Volume scattering is characterized based on Rayleigh theory, analytical Mie diffraction and anomalous diffraction theory (ADT) of van de Hulst [35,36] and Graaff et al. [37]. For absorption at photon energies close to the molecular electronic transition, local disorder, charged states and excitons play a further role. Relevant data were derived using standard dispersion models, such as Tauc-Lorentz [38,39], Tauc-Lorentz-Urbach [40] and excitonic Lorentz oscillator [41–43]. These models are applied to define the wavelength corresponding to the electronic transition energy  $E_g$  between the highest occupied molecular orbital (HOMO) and the lowest unoccupied molecular orbital (LUMO). In order to assign optical scattering to a suitable model,  $R$  &  $T$  measurements were combined with AFM with peak force quantitative nanomechanical mapping (PF-QNM) for determination of surface roughness and inhomogeneity of the materials. We show how optical and mechanical properties are interrelated and must be taken into account for material optimization.

## 2. Experimental

### 2.1. Material

For the model studies, the PU systems resPUR-OT-24000 (PU1) and resPUR-OT (PU2) (produced by resintec GmbH), consisted of the resin base polyester polyol with molecular weight 2300 g/mol for PU1 and 960 g/mol for PU2 (A-components) and different OH-content ( $> 50$  mgKOH/g for

PU1 and  $> 130$  mgKOH/g for PU2), and hexamethylene diisocyanate oligomer (O-HDI) as B component were synthesized. The specification of the discussed PUs is presented in [3] and the relevant parameters are listed in Tab. 1. The mixing ratios A/B (weight) of PU1 and PU2 are 100/20 and 100/60, respectively. For the optical studies, 8 mm thick polymer rods and 10-20  $\mu\text{m}$  thin films on fused silica were prepared, using the same procedure as described in [3].

**Table 1. Characteristic parameters of the investigated PU systems**

Polymer	A-component			B-component	A/B Mixing ratio
	Polyester Polyole	Molecular weight (g/mol)	OH content (mgKOH/g)		
PU 1	P2300	2300	$> 50$	HDI-trimer	100/20
PU 2	P960	960	$> 130$	HDI-trimer	100/60

The properties of the investigated PU elastomers are defined by the covalent bonding of hard- and soft-segments, i.e., oligomers of different chemical compositions and chain flexibility. In general, PUs are synthesized from diisocyanates and oligo-diols by a polyaddition reaction. After polymer formation, hard segments (HS) and soft segments (SS) tend to phase separate, leading to the formation of nano- and microdomains and a morphological superstructure (Fig. 1), and are responsible for optical scattering effects [17–31]. The domain size depends on kinetic and thermodynamic parameters, conditions and method of polymerization, concentration, chemical structure and dimension of the HS. The morphology that is formed primarily depends on the volume fractions of the individual components. If the volume fraction of a component is low, it tends to form spheres. With increasing volume fraction, hexagonal or lamellar structures are formed. For the investigated polymers the hard component, hexamethylene diisocyanate trimer (HDI-trimer), is reacted with the soft component, polyester polyol, with different molecular weight for PU1 and PU2, using aliphatic components. It has a suitable property as required for optical applications, such as high transmission in a wide spectral range. In the case of very long SS chains and low HS content, phase separation and crystallization of SS may occur, resulting in significantly increased scattering. It has a suitable property as required for optical applications, such as high transmission in a wide spectral range. Phase separation and domain formation thus lead to the elastomeric behavior of polyurethanes and essentially determine the optical properties of polyurethanes. As an example of optical scattering in a solid sample of PU with a specific composition, Fig. 2 illustrates the scattering of a green laser beam (wavelength  $\lambda=532$  nm and power  $< 1$  mW) transmitted through 8-mm-thick polymer rods. The photographs are taken perpendicular to the beam axis. For the two different PUs under investigation, it demonstrates different degrees of scattering. A more detailed scattering experiments, carried out in this work, will clarify these test results.

## 2.2. MALDI-TOF

To characterize the polyester polyols (A components), MALDI-TOF mass spectrometry was performed on a Shimadzu AXIMA Confidence mass spectrometer with a nitrogen laser ( $\lambda = 337$  nm). From the observed spectra, the molecular mass distribution was determined to obtain information about the structure of the PUs and their scattering behavior. The polyols were dissolved in a concentration of 3 mg/ml in tetrahydrofuran and 1  $\mu\text{l}$  was applied to a stainless-steel target and allowed to air-dry. For PU1, a mixture of 2-(4'-Hydroxybenzeneazo) benzoic acid (HABA) and  $\alpha$ -cyano-4-hydroxycinnamic acid (CHCA) was used as matrix solution, 5 mg of each substance per ml tetrahydrofuran. For PU2, a solution of 10 mg  $\alpha$ -cyano-4-hydroxycinnamic acid (CHCA) per ml of tetrahydrofuran was used. Mass spectra were measured with an accelerating voltage of 20 kV in positive linear mode. For PU1, a delay time (optimized for 5000 g/mol) was used for pulsed extraction and for PU2, a delay time (optimized for 2000 g/mol) was used in positive

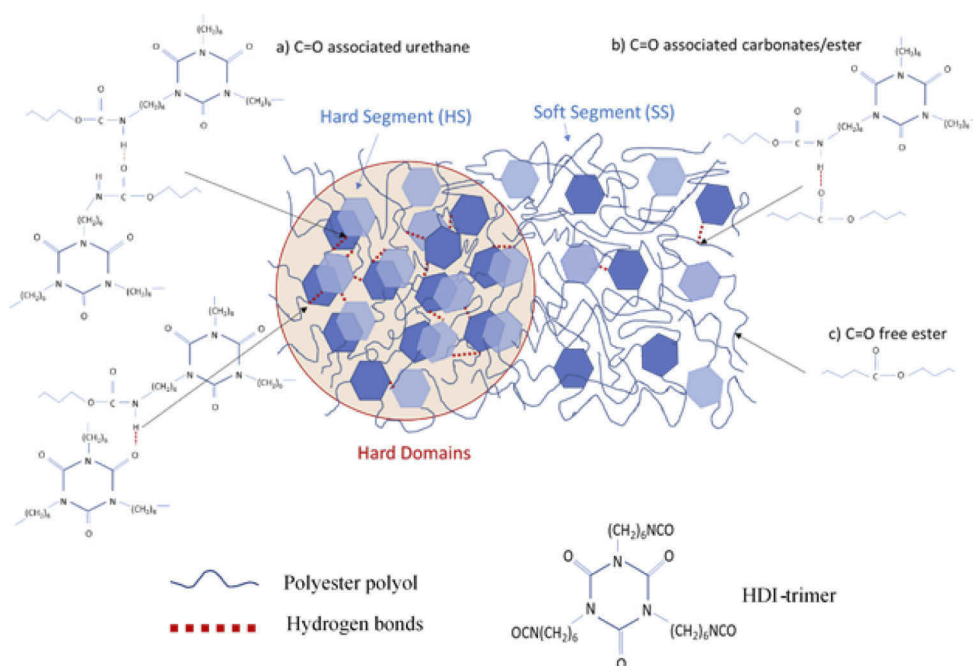


**Fig. 1.** Schematic representation of PU hard domains formation using the one-shot HDI-trimer oligo-diol synthesis method and representation of hydrogen bonds: a) H-bonded C = O associated urethane groups, b) H-bonded C = O associated carbonyl groups and c) free ester C = O groups.

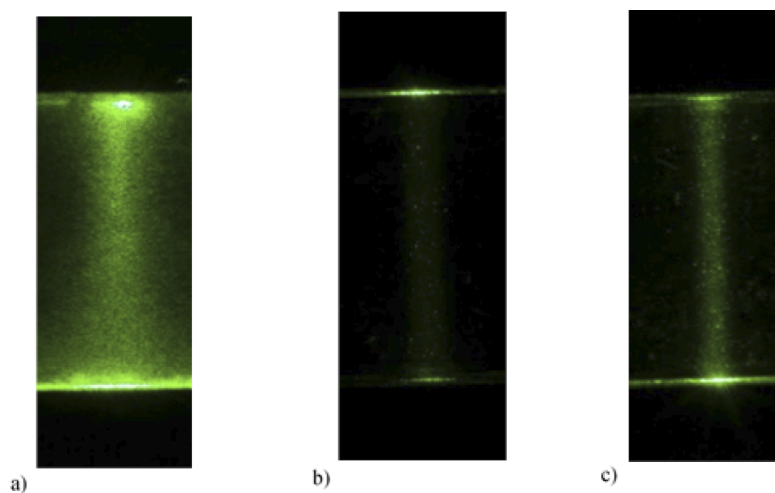


**Fig. 2.** Photos to visualize the different scattering properties of PU1 (a) and PU2 (b, c) taken at right angles to the laser beam axis at a transmission length of 8 mm. The images illustrate increased scattering of PU1 (a) compared to PU2 (b, c). To make the scattering for PU2 clearly visible, the exposure time was increased by a factor of two in (c) compared to (a) and (b).



reflectron mode. 100 profiles per sample with five laser shots accumulated per profile were averaged.

### 2.3. Nanomechanical characterization by AFM

AFM experiments were performed using a Bruker's Dimension Icon. PF-QNM was used to extract the mechanical properties such as indentation, derived from the force-distance curves together with topography. All AFM measurements were performed over areas of  $0.5 \times 0.5 \mu\text{m}^2$  and  $10 \times 10 \mu\text{m}^2$  for observation of microscopic and macroscopic domains segmentations in PUs. The silicon probe RTESPA150 with nominal length, resonance frequency, radius, and spring constant of 125  $\mu\text{m}$ , 150 kHz, 8 nm, and 5 N/m, respectively, was selected and used for  $10 \times 10 \mu\text{m}^2$  scans. ScanAsyst HPI SS silicon nitride probe with nominal length, resonance frequency, radius, and spring constant of 110  $\mu\text{m}$ , 55 kHz, 1 nm, and 0.25 N/m, respectively, was selected and used additionally for high resolution  $0.5 \times 0.5 \mu\text{m}^2$  scans.

### 2.4. Optical investigations

The investigated PUs were analyzed for refractive index  $n$ , extinction coefficient  $k$  and scattering coefficient  $\alpha_s$ . For this purpose,  $R$  &  $T$  measurements were performed in the wavelength range from 200 to 890 nm using different setups and samples with a wide range of thicknesses, as described elsewhere [3]. The overall behavior in absorption and transmission was obtained by a commercial spectrophotometer (Lambda 1050, Perkin Elmer) without any evaluable interference effects due to the relatively low spectral resolution and layer thickness inhomogeneities within the illuminated area of about  $3 \times 3 \text{ mm}^2$ .

The numerical aperture of the measuring beam path is  $<0.05$ . Assuming a cosine-shaped scattering angle distribution, this overestimates the intensity of the transmitted light by a maximum of 1.4%, which has no significant influence on the result within the framework of the present approximation. Transmission and reflection measurements were performed at a normal and near normal (8 deg) angles of incidence, correspondingly, that was defined by measurement tools construction. Thin film interferences were also evaluated to obtain the film thicknesses incorporated in our fitting model. The interference data were obtained by a self-built reflectometer setup (DeepView), as described in [44]. Furthermore, FTIR measurements in the range of 400 - 4000  $\text{cm}^{-1}$  were performed using a 660-IR FT-IR spectrometer (VARIAN, Agilent Technologies) to investigate the morphological structure of the PUs. All optical and AFM measurements were performed on the same samples within markers.

## 3. Models and simulation

### 3.1. Optical fit procedure

To quantify the scattering effect, a scattering coefficient  $\alpha_s$  was defined, so that an effective attenuation coefficient  $\alpha_e$  can be specified by  $\alpha_e = \alpha_a + \alpha_s$ , with the absorption coefficient  $\alpha_a$ .

The parameters  $n(\lambda)$ ,  $\alpha_a(\lambda)$ ,  $\alpha_s(\lambda)$  and film thickness  $d$  were determined with the least squares method from parameterizable models, where experimental (subscript *exp*) and simulated (subscript *sim*) data are compared by  $S_f$  (for thin films) and  $S_r$  (for thick rods) according to

$$S_f = \sum_{\lambda_1}^{\lambda_m} \left( (R_{f \text{ sim}}(n(\lambda), \alpha_e(\lambda), d) - R_{f \text{ exp}}(\lambda))^2 + (T_{f \text{ sim}}(n(\lambda), \alpha_e(\lambda), d) - T_{f \text{ exp}}(\lambda))^2 \right) \quad (1)$$

$$S_r = \sum_{\lambda_1}^{\lambda_m} \left( (R_{r \text{ sim}}(n(\lambda), \alpha_e(\lambda)) - R_{r \text{ exp}}(\lambda))^2 + (T_{r \text{ sim}}(n(\lambda), \alpha_e(\lambda)) - T_{r \text{ exp}}(\lambda))^2 \right). \quad (2)$$

The sum  $S_f + S_r$  is carried out over the wavelength range  $\lambda_1 - \lambda_m$  and minimized by the Levenberg-Marquardt algorithm, using Matlab software.  $R_f$  &  $T_f$  refer to the reflection and transmission

of thin films. Correspondingly,  $R_r$  &  $T_r$  are related to the reflection and transmission of the rods. The calculations of  $R_{fsim}$  and  $T_{fsim}$  for thin films are based on incoherent reflection and transmission within the substrate and coherent superposition of the waves within the thin films, which causes the interference effect (Fig. 3) and can be calculated by [34]

$$R_{fsim} = \frac{R_0 - R_2 T_{sub}^2 (R_1 R_0 - T_1 T_0)}{1 - R_1 R_2 T_{sub}^2} \quad (3)$$

and

$$T_{fsim} = \frac{T_0 T_2 T_{sub}}{1 - R_1 R_2 T_{sub}^2}, \quad (4)$$

where  $R_0$ ,  $T_0$ ,  $R_1$  and  $T_1$  are calculated by the matrix method according to Heavens [45]. The calculation of  $R_2$ ,  $T_2$ ,  $T_{sub}$ ,  $R_{sim}$ , and  $T_{sim}$  is based on Fresnel's equation considering incoherent multiple reflections. The roughness of the surfaces was considered in the Fresnel formulas using scalar diffraction theory by solving the Helmholtz-Kirchhoff integral [32–34].

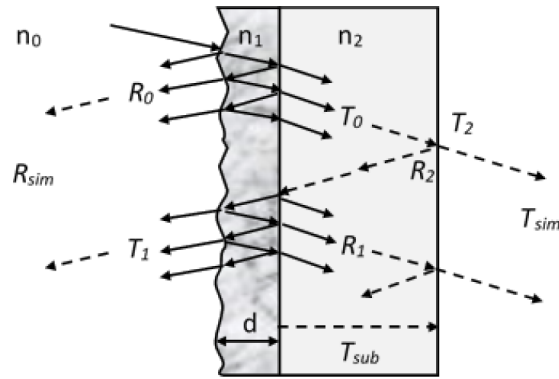


**Fig. 3.** Schematic representation of reflectance  $R_{sim}$  and transmittance  $T_{sim}$  considering the multiple incoherent reflections within the substrate and coherent interference in the inhomogeneous and rough thin film [34].  $R_0$  is the air-side and  $R_1$  is the substrate-side reflectance from the thin film,  $T_0$  is the air-to-substrate and  $T_1$  is the substrate-to-air-side light transmittance through the thin film,  $R_2$  and  $T_2$  are the substrate/air reflectance and transmittance, respectively, and  $T_{sub}$  is the substrate transmittance.

### 3.2. Dispersions models for $n$ and $k$ determination

The optical absorption of polymers can be described by oscillator models [46]. Band gap models such as classical Lorentz oscillators [46–48], and Tauc and Davis-Mott models [47–53] can be used to study the  $\pi$ -orbital transitions of polymers. Lorentz models are often applied for exciton transitions, which, unlike inorganic semiconductors, are largely localized [54]. The models describe the complex dielectric constant  $\epsilon$  of materials and are defined by oscillator parameters. By this parameterization, the optical constants can be determined by the real part  $\epsilon_1 = n^2 - k^2$  and the imaginary part  $\epsilon_2 = 2nk$ , where  $k$  is defined by the absorption coefficient  $\alpha_a = 2\pi k/\lambda$ .

For our investigated materials, we use the Tauc-Lorentz (TL) model [38,39] for the transitions from the ground state (e.g. occupied  $\pi$  and  $\sigma$  orbitals of the polymers) to the excited state (e.g.



unoccupied  $\pi^*$  and  $\sigma^*$  orbitals of the polymers) in accordance with

$$\varepsilon_{2,TL}(E) = \sum_i^N \frac{1}{E} \frac{A_i E_i C_i (E - E_g)^2}{(E^2 - E_i^2)^2 + C_i^2 E^2} \quad E > E_c, \quad (5)$$

where  $A_i$  is the optical oscillator strength,  $C_i$  is the broadening term of the oscillator,  $E_i$  is the inter band critical points (CP) energy and  $E_g$  is the optical band gap energy, equivalent to the transition energy from the HOMO to the LUMO. Bond orders and polymer backbone kinks and the variations of the lattice configuration influence the electronic structure of polymers close to the band gap. Analogous to inorganic materials, this absorption below  $E_g$  can be described by the Urbach tail transitions model [47,55,56]

$$\varepsilon_{2,u}(E) = \frac{A_u}{E} \exp\left(\frac{E}{E_u}\right), \quad 0 < E < E_c \quad (6)$$

integrated into an extended Tauc-Lorentz-Urbach model (TLU) based on [40]. Taking into account the continuity condition of the first derivative of the TL, the following parameters are obtained

$$E_u = (E_c - E_g) \left( 2 - 2E_c(E_c - E_g) \frac{C^2 + 2(E_c^2 - E_0^2)}{C^2 E_c^2 + (E_c^2 - E_0^2)^2} \right)^{-1} \quad (7)$$

and

$$A_u = \exp\left(-\frac{E_c}{E_u}\right) \frac{A E_0 C (E_c - E_g)^2}{(E_c^2 - E_0^2)^2 + C^2 E_c^2}, \quad (8)$$

where  $E_c$  is the connection energy between the two functionalities, which determine the parameters  $E_u$  and  $A_u$  of the Urbach model, shown by Foldyna et al. in [40]. Based on this oscillator model the bandgap  $E_g$ , are determined. In contrast to inorganic semiconductors, the electrons and holes in organic materials are typically localized on the individual molecules and thus form thermally stable Frenkel excitons due to the strong Coulomb interaction [46–48]. In this work, Lorentz distributions [41–43] were used for the exciton transitions, given by

$$\varepsilon_{exc}(E) = \frac{A_{exc} e^{j\Phi_{exc}}}{E - E_{exc} + j\Gamma_{exc}}, \quad (9)$$

where  $A_{exc}$  is the critical-point amplitude,  $E_{exc}$  is the exciton energy threshold and  $\Gamma_{exc}$  is the broadening of the peak. The phase angle  $\Phi_{exc}$  is defined as the angle between the real part ( $E - E_{exc}$ ) and the imaginary part  $\Gamma_{exc}$ , which influences the symmetry of the dielectric function, where  $\Phi_{exc} \rightarrow 0$  at excitonic transitions. The analytical solution for the imaginary part is summarized as follows

$$\varepsilon_2(E) = \varepsilon_{2,TL}(E) + \varepsilon_{2,U}(E) + \varepsilon_{2,exc}(E). \quad (10)$$

The real part  $\varepsilon_{1,TLU}(E)$  of the dielectric function is obtained using analytical integration of the Kramers-Kronig relation

$$\varepsilon_1(E) = \varepsilon_1(\infty) + \frac{2}{\pi} \int_{E_g}^{\infty} \frac{\varepsilon_2(E') E'}{E'^2 - E^2} dE' \quad (11)$$

where  $\varepsilon_1(\infty)$  is the high frequency dielectric constant. The analytical solution of Eq. (11) is given in [38–43].

### 3.3. Determination of the scattering coefficient

The quantification of the scattering  $\alpha_s$  and the absorbing  $\alpha_a$  are based on the investigation of the wavelength dependence of the scattering. By introducing the efficiency factor  $Q$  of a single scatterer, the scattering coefficient  $\alpha_s$  can be defined by

$$\alpha_s = NAQ, \quad (12)$$

where  $N$  is the number density and  $A$  is the geometric cross section of the scattering centers [35,62,63]. In PU, the scattering centers are formed by the domains (Fig. 1). Figure 4 shows schematically the scattering of nano and micro domains which are described by Rayleigh and Mie scattering theory.

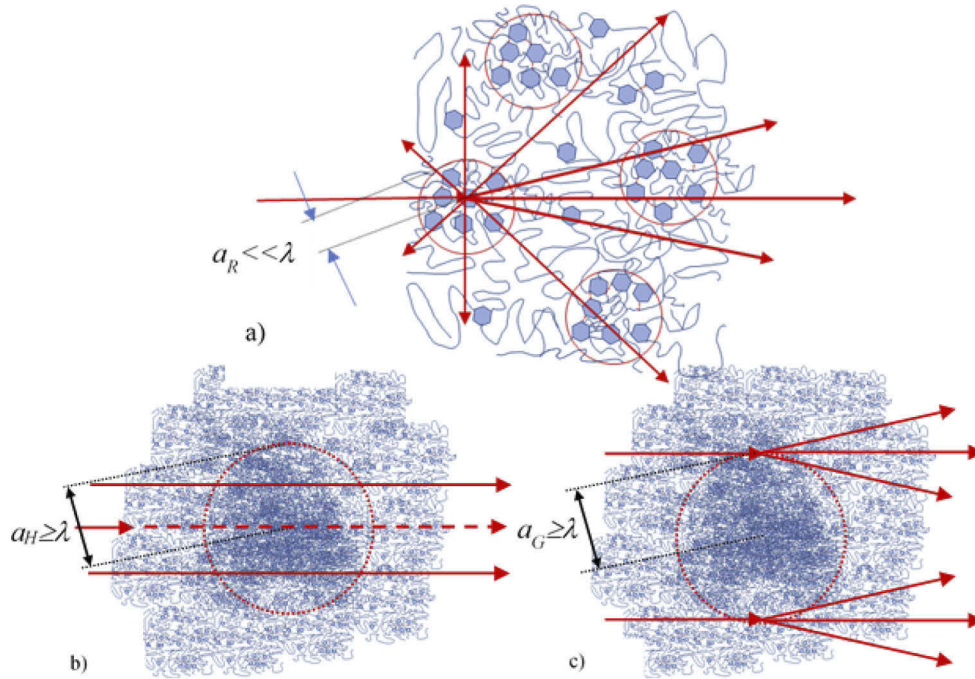


**Fig. 4.** Schematic illustration of a) Rayleigh-, b) the Hulst- and c) the Mie- scattering based on the anomalous and geometrical diffraction theory (ADT). The scattering models used are determined by the radius of the scattering particles, which are formed by a) nano hard domains with the radius of  $a_R$  (Fig. 1) and b), c) macro domains with the radius of  $a_H$  or  $a_G$  for the Mie models of van de Hulst or Graaff, respectively. The macro domains are generated by macroscopic segmentations (long-range density fluctuations) through higher HS contents.

The scattering is determined by the size parameter  $x = 2\pi a/\lambda$ , where  $a$  represents the particle radius and  $\lambda$  is the wavelength, and  $m$  defines the refractive index ratio of the particles and the surrounding medium. Rayleigh scattering theory was applied for particle sizes with  $x_R = 2\pi a_R/\lambda \ll 1$ , where  $a_R$  is the radius of the scattering areas. The efficiency factor depends on the ratio  $m_R$  of the refractive indices of the materials of the scattering domains relative to the environment. According to [35,53,57–61] we can define an efficiency factor  $Q_R$

$$Q_R = \frac{8}{3} \left( \frac{m_R^2 - 1}{m_R^2 + 2} \right)^2 x_R^4, \quad (13)$$

where  $1 < m_R < 1.3$  [35,53,57,59]. Scattering centers with  $x \gg 1$  due to volume inhomogeneities (macro domains) and corresponding refractive index inhomogeneities were treated by Hulst scattering models [53, 57,59], based on a diffraction theory solution of Maxwell's equations for dielectric spheres and van de Hulst model [35], based on ADT model. Thereby different approaches by Graaff et al. [37] and Hulst [35] were considered to find the best approximation to the measurement data. They differ in the treatment of the  $Q$ -factor. The Graaff approximation is derived from Mie diffraction theory with the goal of reducing the oscillations of the solution for  $Q_G$  [37]

$$Q_G = 3.82x_G^{0.37}(m_G - 1)^{2.09}, \quad (14)$$

The factor and exponents given were derived by trial and error in the work of Graaff et al. [37]. for values of  $x$  and  $m$  in the range  $5 < x_G < 50$  and  $1 < m_G < 1.1$ . Another approach to describe the scattering is based on ADT. Here the scattering is primarily caused by the interference of rays that pass through the particle with those that do not (Fig. 4 b). In the ADT model approach, the efficiency factor  $Q$  is expressed by

$$Q_H = 2 \left( 1 - 2 \frac{\sin \rho}{\rho} + 2 \frac{1 - \cos \rho}{\rho^2} \right), \quad (15)$$

where  $\rho = 2x_H(m_H - 1)$  is the phase lag with  $x_H = 2\pi a_H/\lambda$  of a wave travelling along the diameter  $a_H$  as shown in Fig. 4 b. This approximation is valid for non-absorbing spherical scattering centers of  $x_H \gg 1$  and small refractive index ratio compared to the surrounding medium  $|m_H - 1| < 1$  [35,36].

In our approach, the Rayleigh/Graaff model is applied, using an effective damping coefficient of  $\alpha_{eG} = \alpha_{RG} + \alpha_G + \alpha_{aG}$  and the Rayleigh/Hulst model by using  $\alpha_{eH} = \alpha_{RH} + \alpha_H + \alpha_{aH}$ , where  $\alpha_G$  and  $\alpha_H$  are the scattering coefficients of the Graaff and the Hulst models. The effective attenuation coefficient of the Rayleigh/Graaff model is determined by the fit coefficients  $K_R$ ,  $K_G$  and the absorption  $\alpha_{aG}$  by

$$\alpha_{eG} = \alpha_{aG} + \frac{K_R}{\lambda^4} + \frac{K_G}{\lambda^{0.37}}, \quad (16)$$

with the Rayleigh coefficient

$$K_R = 24\pi^3 \left( \frac{m_R^2 - 1}{m_R^2 + 2} \right)^2 V_R \phi_R \quad (17)$$

and Graaff coefficient

$$K_G = 2.46(2\pi)^{0.37} (a_G)^{-0.63} (m_G - 1)^{2.09} \phi_G, \quad (18)$$

where  $\phi_R$  and  $\phi_G$  are the volume fractions per unit volume of the scattering centers, defined by  $\alpha/\phi = (3/4)(Q/a)$  [57]. Analogue follows for the Rayleigh/Hulst model

$$\alpha_{eH} = \alpha_{aH} + \frac{K_R}{\lambda^4} + K_H, \quad (19)$$

with Hulst coefficient

$$K_H = \frac{3}{4a_H} Q_H \phi_H. \quad (20)$$

In the applied models, the scattering areas were approximated by spheres with cross-sections of  $A = \pi a^2$  and corresponding volumes of  $V = 4\pi a^3/3$ . The results of AFM measurements are used as starting values for the fitting procedure. This provides information about the refractive index ratios  $m_G$  and  $m_H$  of hard and soft regions.  $K_R$  is fitted using Rayleigh limit values for scattering particle size parameter ( $x_R = 2\pi a_R/\lambda \ll 1$ ) to determine  $m_R$  using AFM measurements results  $\phi_{RAFM}$  and  $a_{RAFM}$ .

## 4. Results

### 4.1. *Maldi-TOF characterization of polyols*

The molecular weights of polyol were obtained for the two A-components. The mass distribution of the A-component of PU1 indicates a mixture of polyols. We deduced the average molar mass ( $M_n$ ) and the average molecular weight ( $M_w$ ) of the A-components as  $M_n = 2300$  g/mol and  $M_w = 2920$  g/mol for PU1 and  $M_n = 956$  g/mol and  $M_w = 974$  g/mol for PU2, respectively. The polydispersity ( $P = M_w/M_n$ ) for PU1 is  $P \approx 1.3$  and therefore the material has a relatively broad molecular weight distribution compared to PU2 with  $P \approx 1$ .

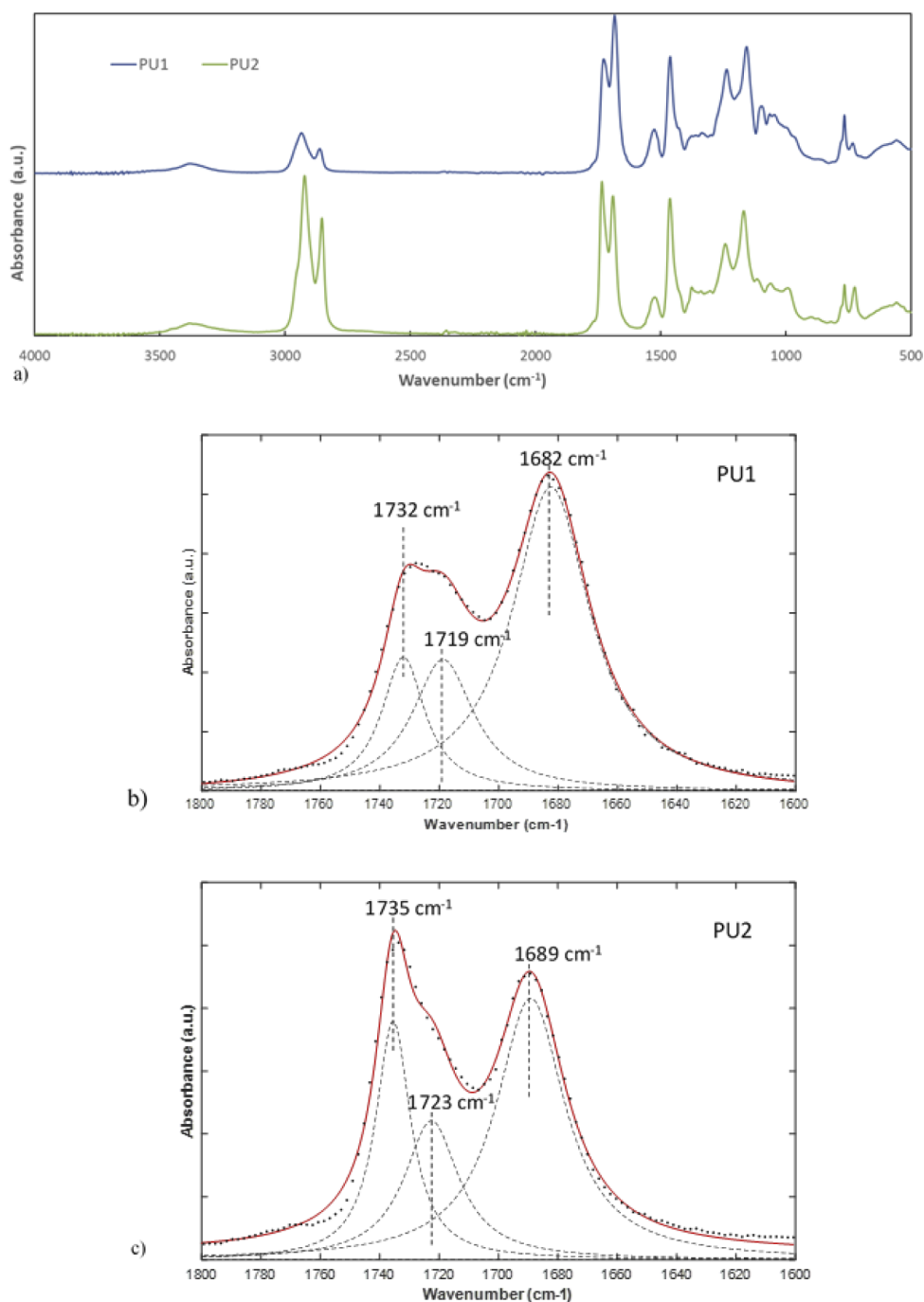
### 4.2. *FTIR spectroscopy*

The FTIR spectra of PU1 and PU2 are shown in Fig. 5. The infrared absorption characteristics of PUs have been investigated in a large number of studies [64–67]. The most important peaks for the studies of the hard segments of PUs are hydrogen-bonded C=O stretching vibrations in the absorption region of  $1600\text{--}1800\text{cm}^{-1}$ . The hydrogen bonded N-H groups are indicated in the range of  $3150\text{--}3550\text{cm}^{-1}$ . The peaks in the range of  $2800\text{--}3000\text{cm}^{-1}$  are due to stretching vibrations of  $\text{CH}_2$  groups, the absorption around  $1460\text{cm}^{-1}$  belongs to deformation vibrations of  $\text{CH}_2$ . The band at  $1520\text{cm}^{-1}$  corresponds to the bending vibration of the N-H bond. The signal at  $1240\text{cm}^{-1}$  is attributed to the C-O and C=O stretching vibrations and the peak at  $1160\text{cm}^{-1}$  can be associated with vibrations of C-O bonds. The absorption band at  $765\text{cm}^{-1}$  can be attributed to the application of HDI-trimer [68,69] and caused by the C-N framework stretching of the cyclic structure. Analysis of hydrogen-bonded C=O stretching absorptions in the range of  $1600\text{--}1800\text{cm}^{-1}$  was performed by Lorentzian deconvolution based on a nonlinear regression using own Matlab program (Fig. 5(b), c). The assignments of the bands describe hydrogen-bonded and “free” (non-hydrogen-bonded) groups. The relatively higher hydrogen bonded urethane associated C=O peak at  $1685\text{cm}^{-1}$ , indicates stronger HS formation and higher phase separation of PU1. Figure 5, in comparison with the studies of Fernández-d’ Arlas et al. [64], shows that the phase separations are formed exclusively by associated urethane carbonyl bands at  $1685\text{cm}^{-1}$ . The peaks of non-hydrogen-bonded C=O groups are at  $1730\text{--}1735\text{cm}^{-1}$ . Figures 1 and 4 schematically show the types of hydrogen-bonded C=O group, H-bonded HS, and SS in the case of the HDI-trimer.

### 4.3. *Peak force quantitative nanomechanical mapping for phase separation observation*

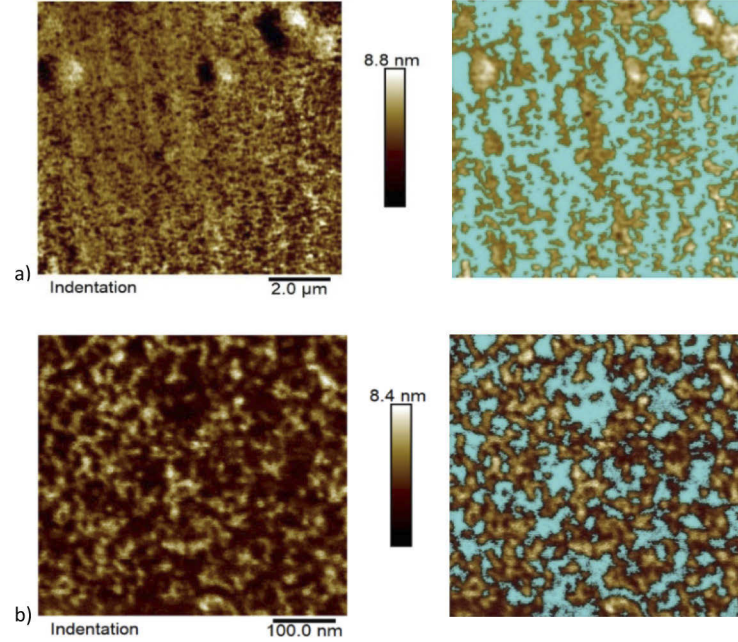
AFM measurements were performed to quantify the density of the scattering components  $\phi$  and the particle size parameters  $x$  that define the light scattering properties according to Eqs. (12)–(20). The results of indentation measurements by PF-QNM are shown in Fig. 6 and Fig. 7 for the PU1 and PU2.  $10 \times 10\text{ }\mu\text{m}^2$  scans were used for determination of the macro domains size of Mie/Hulst models and  $0.5 \times 0.5\text{ }\mu\text{m}^2$  scans were used for determination of Rayleigh scattering nano domain size and the area ratio of nano hard domains to total area. Bruker’s Nanoscope Analysis software was used to perform the domain analysis at a threshold value for the maximum penetration depth (PD). The analytical results are documented in captions of Fig. 6 and 7, and in Tables 3 and 4. The sizes of the nano-domains measured by AFM (Fig. 6 b and 7 b) are approximately the same for both PUs (14–16 nm). These values are in good agreement with literature showing that segmented polyurethane elastomers can exhibit nanoscale phase separations of 2–20 nm determined by the covalent alternating bonding of hard and soft segments, leading to phase separation and domain formation [17–21,28,29,64].

Figure 8 shows the probability distribution of the penetration depth (indentation) of the AFM measurements characterizing the homogeneity of the materials and the density ratio HS/SS. The



**Fig. 5.** FT-IR spectra of PU1 and PU2: a) in the wavenumber range 500-4000  $\text{cm}^{-1}$ . b) and c) show the Lorentzian - deconvoluted FTIR spectrum (dashed measured spectrum, red fitted spectrum) of the C = O stretching vibrations for PU1 and PU2 in the wavenumber range 1600-1800  $\text{cm}^{-1}$ . The bands 1732-1735  $\text{cm}^{-1}$  and 1719-1723  $\text{cm}^{-1}$ , are due to C = O associated free ester (non-hydrogen-bonded) and hydrogen-bonded carbonyl groups, respectively. The hydrogen-bonded HS are located at 1682-1698  $\text{cm}^{-1}$ . The relatively higher peak at 1682  $\text{cm}^{-1}$  for PU1 is related to the increased content of the HS, which correlates with increased scattering.





**Fig. 6.** AFM indentation scans of PU1 thick plates. The green areas show the hard regions of the polymer at the threshold below the maximum of penetration depth. The  $10 \times 10 \mu\text{m}^2$  scan (a) shows macro hard domains with an average radius  $a_{AFM} \sim 404 \text{ nm}$ . The ratio of hard areas to total area is  $\phi_{AFM} \sim 0.57$ . The  $0.5 \times 0.5 \mu\text{m}^2$  scan (b) shows nano hard domains with an average radius  $a_{RAFM} \sim 8.5 \text{ nm}$ . The area ratio of nano hard domains to total area is  $\phi_{RAFM} \sim 0.26$ .

low indentation of PU2 indicates a high homogeneity of the material. Roughnesses (RMS) of 2 nm and 4 nm were determined for the thin PU layers and for the rod material, respectively.

#### 4.4. Optical properties

Figures 9, 10, 11 and 12 show  $R$  &  $T$  spectra of PU thin films and rods. The overall behavior in the wavelength range of 200-890 nm was obtained by the low-resolution spectrophotometer. These reflectance measurements are superposed with high spectral resolution reflectance measurements in the spectral range of 400-600 nm, analogous to [3]. The interferences shown in Figs. 9, 10, 11 and 12 are used for the thickness determination.

**Table 2. R & T fit-parameters of the Tauc-Lorentz-Urbach and excitonic Lorentz oscillator dispersion models (Figs. 9, 10, 12, 13)**

PU1	Model	Tauc-Lorentz					Lorentz- Exciton			
		$E_g$ (eV)	$E_1$ (eV)	$A$ (eV)	$C$ (eV)	$\varepsilon_\infty$	$E_{exc}$ (eV)	$A_{exc}$ (eV)	$\Phi_{exc}$	$\Gamma_{exc}$ (eV)
	Rayleigh/Graaff	4.71	7.7	15.5	0.94	1.9	4.63	4.3E <sup>-4</sup>	0.05	0.17
	Rayleigh/Hulst	4.73	7.6	15.5	0.93	1.9	4.63	4.6E <sup>-4</sup>	0.047	0.19

PU2	Model	Tauc-Lorentz-Urbach							
		$E_g$ (eV)	$E_1$ (eV)	$A$ (eV)	$C$ (eV)	$\varepsilon_\infty$	$E_c$ (eV)	$A_u$ (eV)	$E_u$ (eV)
	Rayleigh/Graaff	4.9	11.1	43	0.81	1.05	5.44	1.82E-12	0.28
	Rayleigh/Hulst	4.88	11.1	42.9	0.8	1.1	5.4	0.79E-12	0.27



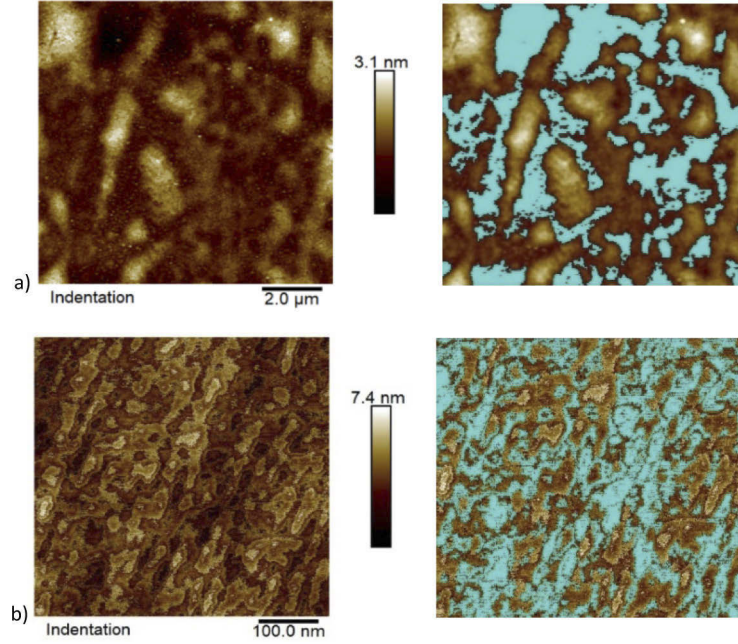


**Fig. 7.** AFM indentation scans of PU2 thick plates. The green areas indicate the hard region of the polymer at the threshold below the maximum penetration depth. The  $10 \times 10 \mu\text{m}^2$  scan (a) shows macro hard domains with an average mean radius  $a_{AFM} \sim 450 \text{ nm}$ . The area ratio of hard area to total area  $\phi_{AFM} \sim 0.37$ . The  $0.5 \times 0.5 \mu\text{m}^2$  scan (b) shows nano hard domains with an average radius  $a_{RAFM} \sim 7 \text{ nm}$  where the area ratio of nano hard domains to total area is  $\phi_{RAFM} \sim 0.33$ .

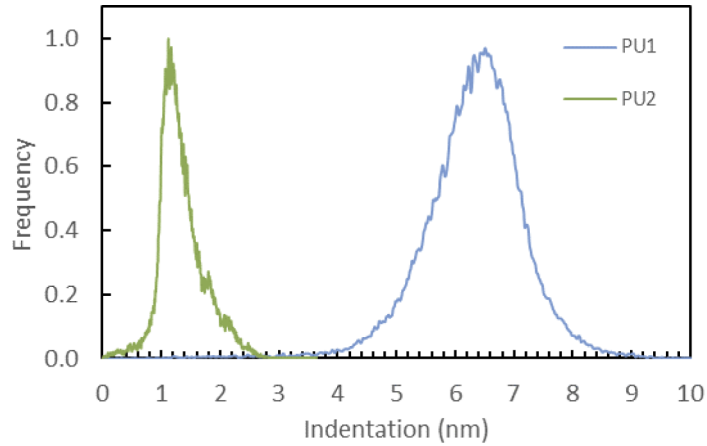


**Fig. 8.** Frequency distribution of the indentation measurements, shown in Figs. 6 a and 7 a.

In order to determine the optical constants, i.e., refractive index  $n$  and extinction coefficient  $k$ , the reflection and transmission simulations were performed with considering roughness and volume scattering. For the initial fit values of the optical dispersion parameters, we use a one-shot fit of the measured values  $R_{fexp}$  &  $T_{fexp}$  of thin films neglecting the scattering analogous to [3]. The fit procedure is performed under the boundary conditions of the models defined in chapter

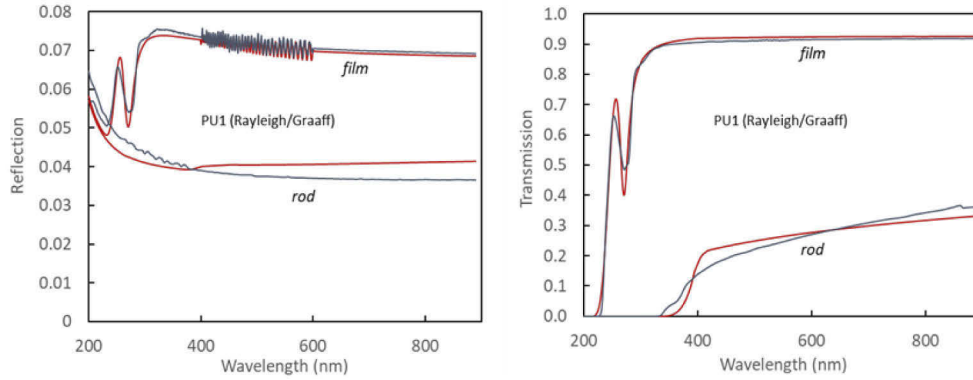


**Fig. 9.**  $R$  &  $T$  fit (red) and measurements (black) for PU1 using the Rayleigh/Graaff model. The rod thickness is 8 mm and the fitted thin film thickness is 14089 nm. The best fit parameters of Rayleigh/Graaff, Tauc-Lorentz and the Lorentz Exciton models are presented in Tables 2–4.

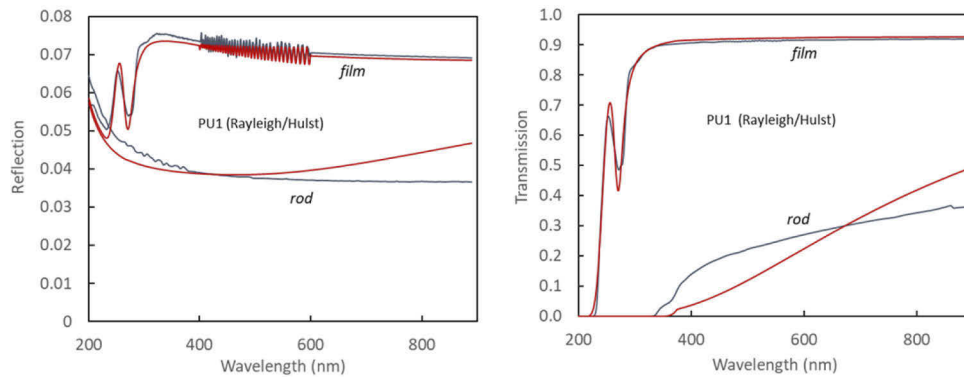


**Fig. 10.**  $R$  &  $T$  fit (red) and measurements (black) for PU1 using Rayleigh/Hulst model. The rod thickness is 8 mm and the fitted thin film thickness is 14099 nm. The best fit parameters of Rayleigh/Hulst, Tauc-Lorentz and the Lorentz Exciton models are presented in Tables 2–4.

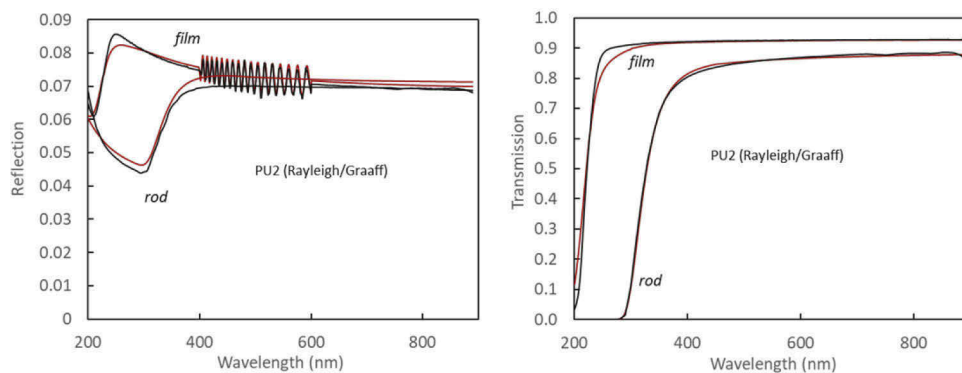


**Fig. 11.**  $R$  &  $T$  fit (red) and measurements (black) for PU2 according to the Rayleigh/Graaff model. The rod thickness is 8 mm and the fitted thin film thickness is 6620 nm. The best fit parameters of Rayleigh/Graaff and Tauc-Lorentz-Urbach models are presented in Tables 2–4.

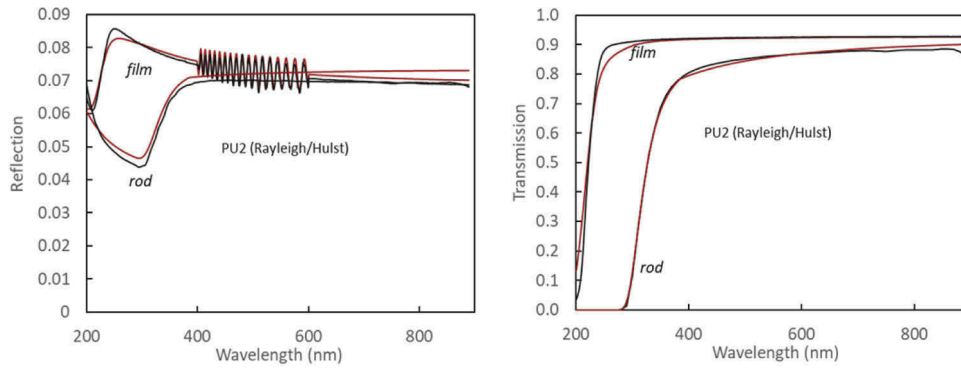


**Fig. 12.**  $R$  &  $T$  fit (red) and measurements (black) for PU2 according to the Rayleigh/Hulst model. The rod thickness is 8 mm and the fitted thin film thickness is 6623 nm. The best fit parameters of Rayleigh/Hulst and Tauc-Lorentz-Urbach models are presented in Tables 2–4.

**Table 3. Comparison of  $R$  &  $T$  fit using Mie/Hulst scattering and AFM results**

	Model	$R$ & $T$ fitting (Figs. 9, 10, 11, 12)			AFM ( $10 \times 10 \mu\text{m}^2$ scan) (Figs. 6(a), 7(a))		
		$a_G, a_H^b$ (nm)	$m_G, m_H^b$	$\phi_G, \phi_H^b$	$a_{AFM}$ (nm)	$\phi_{AFM}$	$PD^a$ (nm)
PU1	Rayleigh/Graaff	$a_{AFM}=404$	1.006	$\phi_{AFM}=0.57$	404	0.57	8.0
	Rayleigh/Hulst	530	1.002	0.51			
PU2	Rayleigh/Graaff	$a_{AFM}=450$	1.001	$\phi_{AFM}=0.37$	450	0.37	3.1
	Rayleigh/Hulst	301	1.0005	0.44			

<sup>a</sup>PD-penetration depth demonstrated by a color bar of Figs. 6(a) and 7(a).

<sup>b</sup>Rayleigh/Graaff model subscript  $G$ , Rayleigh/Hulst model subscript  $H$

**Table 4. Relative index of refraction  $m_R$  of Rayleigh scattering**

	Model	$R$ & $T$ fitting (Figs. 10, 11, 12, 13)	AFM ( $0.5 \times 0.5 \mu\text{m}^2$ scan) (Figs. 6(b), 7(b))			$m_R$ (calculated from Eq. (17))
		$K_R$ (nm <sup>3</sup> )	$a_{RAFM}$ (nm)	$\phi_{RAFM}$	$PD^a$ (nm)	
PU1	Rayleigh/Graaff	142	8.5	0.26	8.4	1.45
	Rayleigh/Hulst	110				1.30
PU2	Rayleigh/Graaff	96	7	0.33	7.4	1.25
	Rayleigh/Hulst	75				1.2

<sup>a</sup>PD-penetration depth demonstrated by a color bar of Figs. 6(b) and 7(b).

3 under consideration of the AFM indentation results  $a_{AFM}$  and  $\phi_{AFM}$ . The fitting procedure provides the optical dispersion parameters shown in Tab.2 together with the scattering parameters shown in Tabs. 3 and 4 as well as the film thickness  $d$ . The corresponding fit curves in Figs. 9, 10, 11 and 12 are marked red. The best fit was obtained with the Rayleigh/Graaff model for the thin films (Figs. 9 and 10). The results of effective damping, absorption and scattering coefficients are shown in Figs. 13 and 14 by using the Rayleigh/Graaff and Rayleigh/Hulst scattering model. Using the particle diagnostics of the AFM measurements (Figs. 6 b and 7 b) and Rayleigh parameters (Tab. 4), the refractive index ratio  $m_R$  can be calculated from Eq. (17). The optical constants  $n$  and  $k$  with and without consideration of the scattering effect are shown in Fig. 15 in comparison.

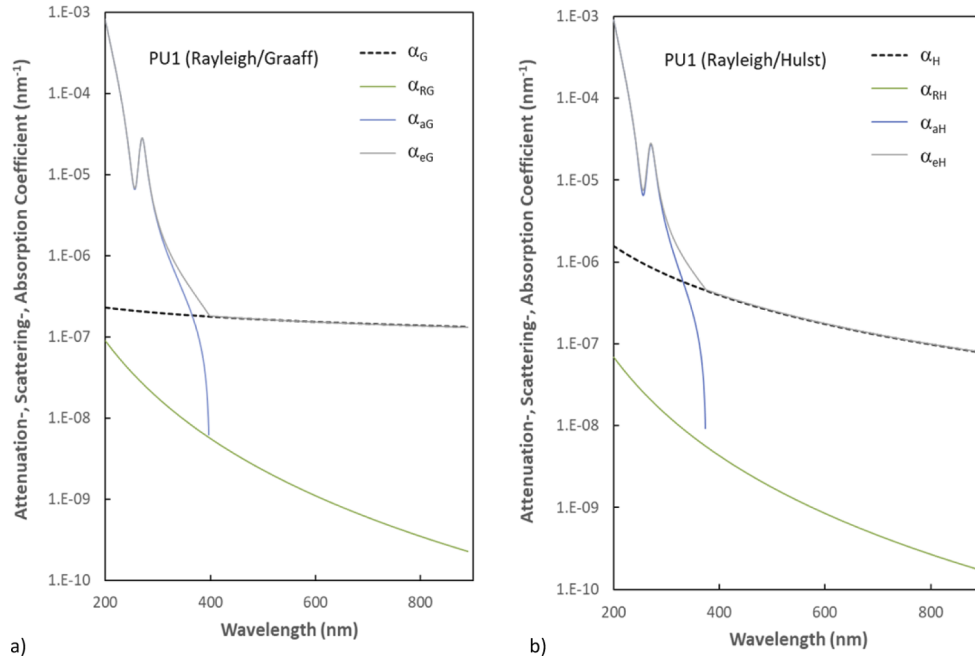


**Fig. 13.** Fitted absorption and scattering coefficients for PU1 according to the Rayleigh/Graaff (a) and Rayleigh/Hulst model (b).

As a main result, it can be concluded that all parameters satisfy the boundary conditions of the Graaff ( $5 < x_G < 50$ ,  $1 < m_G \leq 1.1$ ), Hulst ( $x_H \gg 1$  and  $|m_H - 1| \ll 1$ ) and the Rayleigh ( $1.0 < m_R \leq 1.3$ ,  $0 < x_R \leq 0.3$ ) scattering models.

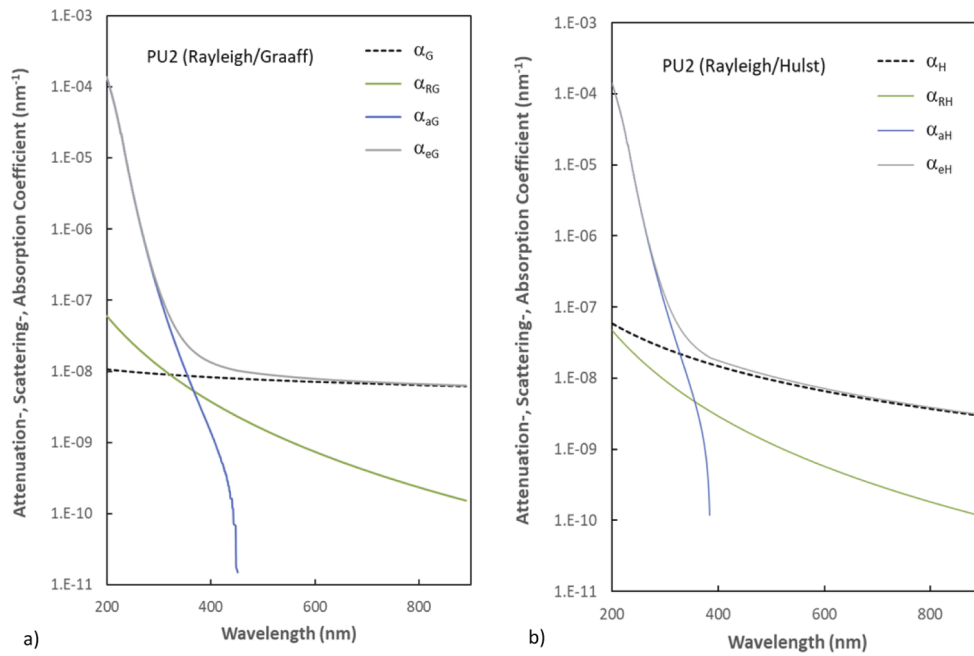


**Fig. 14.** Fitted absorption and scattering coefficients for PU2 according to the Rayleigh/Graaff (a) and Rayleigh/Hulst model (b).

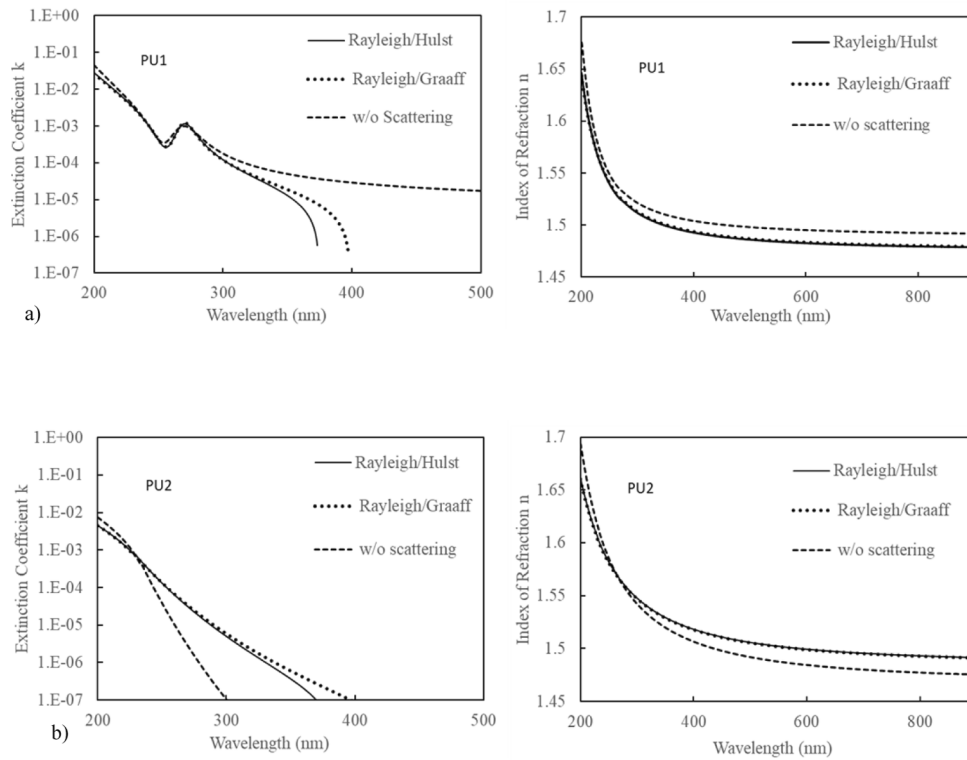


**Fig. 15.** Extinction coefficient  $k$  and refractive index  $n$  for PU1 (a) and PU2 (b) evaluated without and with consideration of scattering using the Rayleigh/Hulst and Rayleigh/Graaff models. The determination of the optical constants without consideration of scattering is based on  $R$  &  $T$  measurements of thin films only. Applying the Rayleigh/Graaff and the Rayleigh/Hulst model, the differences for the refractive index are negligible.



## 5. Discussion

The AFM results in Figs. 6 and 7 show the typical behavior of phase separation and domain formation of PUs in the scanning range of  $10 \times 10 \mu\text{m}^2$  and  $0.5 \times 0.5 \mu\text{m}^2$ . The models of segmentation described by Ginzburg et al. [31], Allport et al. [70], Hepburn [71], Fernández d' Arlas et al. [64], He et al. [67] are shown schematically in Figs. 1 and 4 for the PUs under investigation. AFM measurements (Figs. 6 b and 7 b) in the scan range of  $0.5 \times 0.5 \mu\text{m}^2$  show domain formation with dimensions of 15-20 nm which is also confirmed theoretically by the application of the Rayleigh scattering model and is analogous to the results of [64]. These hard domains are formed by self-assembled covalent bonds of urethane hydrogen bonds of  $\text{NH C}=\text{O}$  groups also forming more ordered or crystalline structures. The thermodynamic incompatibility between the polar HS and the less polar SS makes the Gibbs free energy positive, and forces it to phase separate [67]. Figure 7 b shows cylindrical structures for the PU2 in contrast to more spherical structures of the PU1 (Fig. 6 b). Garret et al. [21], and He et al. [67] show that, longer structures form at higher mixing ratios of the hardener component due to lower mixing entropy, which is the case for the PU2. The  $10 \times 10 \mu\text{m}^2$  AFM scans show microscopic segmentations (long-range density fluctuations) in the dimension of 400-500 nm (Figs. 6 a and 7 a). The segmentation is in the order of the investigated wavelength and causes scattering that can be described by Mie/Hulst scattering models. Comparison of Fig. 13 with Fig. 14 shows that the scattering coefficients  $\alpha_G$  and  $\alpha_H$  of PU1 are an order of magnitude higher than those of PU2. We explain the increased scattering effect in PU1 by the formation of microscopic structures with higher scattering potential due to the increase of the ratio of the refractive indices  $m$  ( $m_G$  and  $m_H$ ) and the volume fraction  $\phi$  (see Table 3). The effect of differences in domain structure between PU1 and PU2 is also confirmed by the FTIR measurements. The FTIR spectra and Lorentzian deconvolution (Fig. 5) show a higher  $\text{C}=\text{O}$  hydrogen peak, corresponding to hydrogen bonds associated with urethane ( $1685 \text{ cm}^{-1}$ ), indicating stronger HS formation and higher phase separation of PU1. This correlates with AFM results (Figs. 6 a and 7 a). In contrast, the non-hydrogen-bonded  $\text{C}=\text{O}$  groups (free carbonates and ethers) at  $1730\text{-}1735 \text{ cm}^{-1}$  in PU2 indicate less phase separation.

Comparison of the results of AFM, FTIR and MALDI-TOF measurements indicates that the degree of phase separation in PU increases with the molecular weight of the polyol. We assume, that the differences in domain structure between PU1 and PU2 are mainly caused by  $M_n$  and  $P$  in agreement with Lan et al. [72] and Silver et al. [73].

The results of  $R$  &  $T$  measurements and their fit to the scattering models support this interpretation of the polymer morphology. We found that nano domains have higher  $m$ -values than the micro domains indicating stronger hydrogen bonding of the nano domains (Table 3 and 4). The equality of the  $m_R$  values of the two PUs show that the hard phase domain formation of both polymers and the Rayleigh scattering properties are approximately the same. Therefore, the higher scattering of PU1 compared to PU2 can be mainly explained by the higher phase separation of the PU1 micro domains, which is determined by the higher refractive index ratio ( $m_G$ ,  $m_H$  and  $m_R$ ) of PU1 and also by the penetration depth (Fig. 6 a). This is also indicated by the broader molecular weight and intension distribution (Fig. 7) of PU1. In other words, broad molecular weight distribution (higher  $P$ ) of polyols of PU1 cause higher  $PD$  ( $PD_{PU1}=8.8 \text{ nm}$ ,  $PD_{PU2}=3.1 \text{ nm}$ ) and phase separation distribution of hard and soft components.

The results of optical characterization of the polymers based on  $R$  &  $T$  measurements considering Mie/Hulst and Rayleigh scattering and fit initial values of domain size from AFM analysis show that the optical absorptions can be determined separately from the scattering coefficients. This is shown in Figs. 11 and 15. The best-fit results to the  $R$  &  $T$  measurements of the dispersion model parameters and the scattering models are shown in Figs. 9, 10, 12, and 13. In these investigations, the Rayleigh/Graaff model proves to be more suitable than the Rayleigh/Hulst model, which is particularly visible in the case of the high scattering material

(Fig. 10). As shown in Table 2, the analyzed resin films exhibit band gap energies  $E_g$  of 4.71 and 4.73 eV for PU1, and 4.90 and 4.88 eV for PU2 are being similar for both scattering models. The transmission attenuation peaks of PU1 at the wavelength of  $\lambda \approx 270$  nm in Figs. 9 b and 10 b can be explained by exciton transitions with energies of  $E_{exc} = 4.63$  eV, and influence on the dielectric constants in the range below  $E_g$ . Figures 11 and 14 show  $\alpha_s$ ,  $\alpha_a$  und  $\alpha_R$  as a part of the effective attenuation coefficient  $\alpha_e$ . For the material with high scattering (PU1), Rayleigh scattering is negligible. Figure 15 shows the dispersion of the optical constants  $n$  and  $k$  of PUs under consideration of the scattering parameters. Comparing both scattering models in the full wavelength range of 200-890 nm, we obtain differences of up 10% for the extinction coefficient. In contrast, differences in the refractive index are negligible. In general, the Rayleigh/Graaff model shows better goodness of fit. Comparison of the optical constants determined only from  $R$  &  $T$  measurements of thin films on quartz substrate without consideration of the scattering models is depicted as dashed lines in Fig. 15, which indicates that consideration of the scattering effect is important for the correct determination of the  $k$ -values for increased scattering thin films in the long wavelength range where  $k < 10^{-3}$  (Fig. 15 a). It is essential that the exact determination of the  $k$ -values for the PUs in the range of photon energies below  $E_g$  can only be determined by measuring thick samples. Based on these results and from the comparison of Figs. 6 b and 7 b (lower indentation in PU2), it can be concluded that the PU2 is very homogeneous, in terms of microscopic phase separation, resulting in very low scattering, as also indicated in Fig. 2, making it suitable for applications in optics and optoelectronics.

As the results presented here, we proposed and experimentally verified a new method for simultaneous determination of dielectric constants and scattering properties of polymers for optoelectronic applications using combination of optical  $R$  &  $T$  measurements in connection with a parametric modeling procedure. A more complex numerical treatment of radiative transfer, based on multiple transport theory or a rigorous solution of Maxwell's equations, can in principle provide more accurate solutions, but requires adapted optical setups and is rather time consuming.

## 6. Conclusion

The application of optical functional polymers requires knowledge of optical constants and light scattering properties. In this work, the optical constants and the scattering coefficients were determined from the reflection and transmission measurements of thin films and rods in the wavelength range from 200 to 890 nm on the basis of dielectric dispersion and analytical scattering models. Rayleigh, Mie and Hulst scattering models were used to characterize the scattering due to volume inhomogeneities and the scalar diffraction theory due to surface roughness. Atomic force microscopy with peak force quantitative nanomechanical mapping was applied to extract the topography as well as mechanical properties such indentation depth in order to assign the optical scattering to a suitable model.

We found that the scattering is primarily caused by the size of the microdomains and their refractive index ratios, which are related to the molecular weight of the polyols. For accurate determination of optical constants and band structure parameters, it is essential to consider scattering in the models. Even with low scattering, its consideration is important, especially for polymer optics and other thick samples. The described method appears to be well suited for the qualification of new polymer materials. It can help develop high-performance optical polymers for the lighting industry to minimize scattering losses and increase illumination efficiency.

**Funding.** Bundesministerium für Wirtschaft und Energie ((16KN074923)).

**Disclosures.** The authors declare that there are no conflicts of interest related to this article.

**Data availability.** Data underlying the results presented in this paper are not publicly available at this time but may be obtained from the authors upon reasonable request.

## References

1. Stefan Bäumer, *Handbook of Plastic Optics* (Wiley-VCH Verlag GmbH & Co. KGaA, 2010).
2. Hans-Georg Elias, *Makromoleküle*, Band 4, Anwendungen von Polymeren (WILEY-VCH Verlag GmbH & Co. KGaA, 2003).
3. J. Bauer, M. Gutke, F. Heinrich, M. Edling, V. Stoycheva, A. Kaltenbach, M. Burkgardt, M. Gruenefeld, M. Gamp, C. H. Gerhard, P. Steglich, S. Steffen, M. Herzog, C. H. Dreyer, and S. Schrader, "Novel UV-transparent 2-component polyurethane resin for chip-on-board LED microlenses," *Opt. Mater. Express* **10**(9), 2085–2099 (2020).
4. P. Tollay, "Polymer optics gain respect," *Photon. Spectra* **37**, 76 (2003).
5. K. Angermaier and P. H. Müller, "*UV-härtende Silicone*," Carl Hanser Verlag, München, *Kunststoffe* **4** (2010).
6. W. M. Lee, A. Upadhyay, P. J. Reece, and T. G. Phan, "Fabricating low cost and high-performance elastomer lenses using hanging droplets," *Biomed. Opt. Express* **5**(5), 1626 (2014).
7. C.-L. C. Chien, S.-F. Yu-Che Huang, C.-M. Chang, M.-C. Yip, and W. Fang, "Polymer dispensing and embossing technology for the lens type LED packaging," *J. Micromech. Microeng.* **23**(6), 065019 (2013).
8. R. Yoshimura, M. Hikoto, S. Tomaru, and S. Imamura, "Low-loss polymeric optical waveguides fabricated with deuterated polyfluoromethacrylate," *J. Lightwave Technol.* **16**(6), 1030–1037 (1998).
9. T. Matsuura, S. Ando, S. Sasaki, and F. Yamamoto, "Polyimides derived from 2,2'-Bis(trifluoromethyl)-4,4'-diaminobiphenyl. 4. optical properties of fluorinated polyimides for optoelectronic components," *Macromolecules* **27**(22), 6665–6670 (1994).
10. H. J. Lee, M. H. Lee, M. C. Oh, J. H. Ahn, and S. G. Han, "Crosslinkable polymers for optical waveguide devices. II. Fluorinated ether ketone oligomers bearing ethynyl group at the chain end," *J. Polym. Sci., Part A: Polym. Chem.* **37**(14), 2355–2361 (1999).
11. J. W. Kang, J. P. Kim, W. Y. Lee, J. S. Kim, J. S. Lee, and J. J. Kim, "Low-loss fluorinated poly(arylene ether sulfide) waveguides with high thermal stability," *J. Lightwave Technol.* **19**(6), 872–875 (2001).
12. G. Fischbeck, R. Moosburger, C. Kostzewa, A. Aeben, and K. Petermann, "Singlemode optical waveguides using a high temperature stable polymer with low losses in the 1.55  $\mu\text{m}$  range," *Electron. Lett.* **33**(6), 518 (1997).
13. M.-C. Oh, K.-J. Kim, W.-S. Chu, J.-W. Kim, J.-K. Seo, Y.-O. Noh, and H.-J. Lee, "Integrated photonic devices incorporating low-loss fluorinated polymer materials," *Polymers* **3**(3), 975–997 (2011).
14. C. Dreyer, J. Schneider, K. Göcks, B. Beuster, M. Bauer, N. Keil, H. Yao, and C. Zawadzki, "New reactive polymeric systems for use as waveguide materials in integrated optics," *Macromol. Symp.* **199**(1), 307–320 (2003).
15. L. M. Goldenberg, M. Koehler, O. Kahle, and Chr. Dreyer, "Impact of inorganic nanoparticles on optical properties of low refractive index waveguiding polymers," *Opt. Mater. Express* **10**(11), 2987–2997 (2020).
16. O. Ziemann, J. Krauser, P. E. Zamzow, and W. Daum, *Optical Short Range Transmission Systems*, (Springer-Verlag Berlin Heidelberg, 2008).
17. G. Festel, A. Goë Idel, and C.D. Eisenbach, "Morphologische Untersuchungen an segmentierten Polyurethan Elastomeren auf Basis von Naphthalin-1,5-diisocyanat," *Elastomere und Kunststoffe, KGK Kautschuk Gummi Kunststoffe* **53**(3), (2000).
18. R. Bonart, "Thermoplastic elastomers," *Polymer* **20**(11), 1389–1403 (1979).
19. R. Bonart, "X-ray investigations concerning the physical structure of cross-linking in segmented urethane elastomers," *J. Macromol. Sci., Part B: Phys.* **2**(1), 115–138 (1968).
20. J. T. Garrett, J. Runt, and J. S. Lin, "Microphase separation of segmented poly(urethane urea) block copolymers," *Macromolecules* **33**(17), 6353–6359 (2000).
21. J. T. Garrett, J. Runt J, and C. A. Siedlecki, "Microdomain morphology of poly(urethane urea) multiblock copolymers," *Macromolecules* **34**(20), 7066–7070 (2001).
22. M. J. O'Sickey, B. D. Lawrey, and G. L. Wilkes, "Structure-property relationships of poly(urethane urea)s with ultra-low monol content poly(propylene glycol) soft segments. I. Influence of soft segment molecular weight and hard segment content," *J. Appl. Polym. Sci.* **84**(2), 229–243 (2002).
23. E. Tocha, H. Janik, M. Debowski, and G. J. Vancso, "Morphology of PU Revisited by Complementary AFM and TEM," *J. Macromol. Sci., Part B: Phys.* **41**(4-6), 1291–1304 (2002).
24. F. M. Sonnenschein, *PU Science, Technology, Markets, and Trends*, (John Wiley & Sons, Inc 2015).
25. H. Younes and D. Cohn, "Phase separation in poly(ethylene glycol)/poly(lactic acid) blends," *Eur. Polym. J.* **24**(8), 765–773 (1988).
26. C. Vogel, E. Wessel, and H. W. Siesler, "FT-IR imaging spectroscopy of phase separation in blends of poly(3-hydroxybutyrate) with poly (l-lactic acid) and poly (ε-caprolactone)," *Biomacromolecules* **9**(2), 523–527 (2008).
27. D. Joel and A. Hauser, "Thermal dissociation of urethanes studied by FTIR spectroscopy," *Angew. Makromol. Chem.* **217**(1), 191–199 (1994).
28. S. Schrader, X. Li, F. Guo, Y. Liu, J. Luo, and D. Xu, "Electron microscopy investigation of Polyester-polyurethane elastomers stained with ruthenium tetroxide," *Makromol. Chem., Rapid Commun.* **9**(9), 597–601 (1988).
29. R. Bonart, L. Morbitzer, and G. Hentze, "X-ray investigations concerning the physical structure of cross-linking in urethane elastomers. II. Butanediol as chain extender," *J. Macromol. Sci., Part B: Phys.* **3**(2), 337–356 (1969).
30. C. Tsonos, L. Apekis, K. Viras, L. Stephanenko, L. Karabanova, and L. Sergeeva, "Investigation of the Microphase Separation in Blends of Polyurethane-Based Ionomers," *J. Macromol. Sci., Part B: Phys.* **39**(2), 155–174 (2000).
31. V. V. Ginzburg, J. Bicerano, Ch. P. Christenson, A. K. Schrock, and A. Z. Patashinski, "Modeling Mechanical Properties of Segmented PU," in *Nano- and Micromechanics of Polymer Blends and Composites* (Carl Hanser Verlag GmbH & Co., 59–89 2009).

32. P. Beckmann and A. Spizzichino, *The Scattering of Electromagnetic Waves from Rough Surfaces*, (Pergamon, 1963).
33. I. Ohlidal, K. Navratil, and F. Lukes, "Reflection of light by a system of nonabsorbing isotropic film–nonabsorbing isotropic substrate with randomly rough boundaries," *J. Opt. Soc. Am.* **61**(12), 1630 (1971).
34. J. Bauer, "Bestimmung der optischen Konstanten, der Schichtdicke und der Oberflächenrauigkeit dünner Schichten," *Experimentelle Technik der Physik* **25**(2), 105–116 (1977).
35. H. C. van de Hulst, *Light Scattering by Small Particles* (Wiley, 1957).
36. Y. I. Granovskii and M. Stoh, "Attenuation of light scattered by transparent particles," *JETP* **78**(5), 645 (1994).
37. R. Graaff, J. G. Aarnoudse, J. R. Zijp, P. M. A. Sloot, F. F. M. de Mul, J. Greve, and M. H. Koelink, "Reduced light-scattering properties for mixtures of spherical particles: a simple approximation derived from Mie calculations," *Appl. Opt.* **31**(10), 1370 (1992).
38. G. E. Jellison and F. A. Modine, "Parameterization of the optical functions of amorphous materials in the interband region," *Appl. Phys. Lett.* **69**(3), 371–373 (1996).
39. G. E. Jellison and F. A. Modine, "Erratum," *Appl. Phys. Lett.* **69**(14), 2137 (1996).
40. M. Foldyna, K. Postava, J. Bouchala, J. Pitara, and T. Yamaguchi, "Model dielectric function of amorphous materials including Urbach tail," *Proc. SPIE* **5445**, 301–305 (2003).
41. M. Cardona, *Modulation Spectroscopy*, Suppl. vol. 11 to *Solid State Physics*, F. Seitz, D. Turnbull, and H. Ehrenreich, eds. (Academic, 1969).
42. P. Lautenschlager, M. Garriga, S. Logothetidis, and M. Cardona, "Interband critical points of GaAs and their temperature dependence," *Phys. Rev. B* **35**(17), 9174–9189 (1987).
43. D. E. Aspnes, "Modulation spectroscopy/electric field effects on the dielectric function of semiconductors," in *Handbook of Semiconductors*, Vol. 2, M. Balkanski, ed. North-Holland, 109–154 (1980).
44. J. Bauer, O. Fursenko, S. Marschmeyer, F. Heinrich, S. Pulwer, P. Steglich, C. Villringer, A. Mai, and S. Schrader, "Very high aspect ratio through silicon via reflectometry," *Proc. SPIE* **10329**, 103293J–1 (2017).
45. O. S. Heavens, *The Optical Properties of Thin Solid Films*, (Butterworth, 1955).
46. A. Köhler and H. Bässler, "Electronic processes in organic semiconductors," in *The Electronic Structure of Organic Semiconductors* (Wiley-VCH Verlag GmbH & Co, 2015).
47. A. N. Alias, Z. M. Zabidi, A. M. M. Ali, M. K. Harun, and M. Z. A. Yahya, "Optical characterization and properties of polymeric materials for optoelectronic and photonic applications," *International Journal of Applied Science and Technology* **3**, 5 (2013).
48. A. B. Djurisić, T. Fritz, and K. Leo, "Modelling the optical constants of organic thin films: impact of the choice of objective function," *J. Opt. A: Pure Appl. Opt.* **2**(5), 458–464 (2000).
49. D. K. Seo and R. Hofmann, "Direct and indirect band gap types in one-dimensional conjugated or stacked organic materials," *Theor. Chem. Acc.* **102**(1-6), 23–32 (1999).
50. N. F. Mott and E. A. Davis, *Electronic Processes in Non-crystalline Materials* (Oxford University, 1971).
51. A. N. Alias, Z. M. Zabidi, A. M. M. Ali, M. K. Harun, and M. Z. A. Yahya, "Optical Characterization of Luminescence Polymer Blends Using Tauc/Davis-Mott Model," *Adv. Mater. Res.* **488–489**, 628–632 (2012).
52. J. Tauc, "Optical Properties of Amorphous Semiconductor," in *Amorphous and Liquid Semiconductor* (Plenum Publishing Company LTD, 1973).
53. N. L. Dmitruk, A. V. Goncharenko, and E. F. Venger, *Optics of Small Particles and Composite Media* (Naukova Dumka Kyiv, 2009).
54. W. Brütting and W. Rieß, "Grundlagen der organischen Halbleiter," *Physik Journal* **7**, 33 (2008).
55. D. A. Tahir, "Optical properties of polymer composite PS-PC thin films," *Journal of Kirkuk University –Scientific Studies* **5**(2), 87 (2010).
56. A. S. Abed, K. M. Ziadán, and A. Q. Abdullah, "Some optical properties of polyurethane," *Iraqi J. of Polymers* **17**(1), 18 (2014).
57. M. Kerker, *The Scattering of Light and other Electromagnetic Radiation* (Academic 1969).
58. W. Heller, "Theoretical investigations on the light scattering of sphere: range of practical validity of the Rayleigh theory," *J. Chem. Phys.* **42**(5), 1609–1615 (1965).
59. C. F. Bohren and D. R. Huffman, *Absorption and Scattering of Light by Small Particles* (John Wiley & Sons, Inc. 1983).
60. V. V. Tuchin, "Polarized light interaction with tissues," *J. Biomed. Opt.* **21**(7), 071114 (2016).
61. D. W. Hahn, *Light Scattering Theory*, Dissertation, Department of Mechanical and Aerospace Engineering, University of Florida (2009).
62. J. R. Mourant, T. Fuselier, J. Boyer, T. M. Johnson, and I. J. Bigio, "Predictions and measurements of scattering and absorption over broad wavelength ranges in tissue phantoms," *Appl. Opt.* **36**(4), 949 (1997).
63. A. M. K. Nilsson, C. Sturesson, D. L. Liu, and S. Andersson-Engels, "Changes in spectral shape of tissue optical properties in conjunction with laser-induced thermotherapy," *Appl. Opt.* **37**(7), 1259 (1998).
64. B. Fernández-d'Arlas, L. Rueda, R. Fernández, U. Khan, J. N. Coleman, I. Mondragon, and A. Eceiza, "Inverting polyurethanes synthesis: effects on nano/micro-structure and mechanical properties," *Soft Mater.* **9**(1), 79–93 (2010).
65. T. Gurunathan, S. Mohanty, and S. K. Nayak, "Isocyanate terminated castor oil-based polyurethane prepolymer: synthesis and characterization," *Prog. Org. Coat.* **80**, 39–48 (2015).
66. J. Mattia and P. Painter, "A comparison of hydrogen bonding and order in a polyurethane and poly(urethane-urea) and their blends with poly(ethylene glycol)," *Macromolecules* **40**(5), 1546–1554 (2007).

67. Y. He, D. Xie, and X. Zhang, "The structure, microphase-separated morphology, and property of polyurethanes and polyureas," *J. Mater. Sci.* **49**(21), 7339–7352 (2014).
68. Y. Zhang, J. Maxted, A. Barber, C. Lowe, and R. Smith, "The durability of clear polyurethane coil coatings studied by FTIR peak fitting," *Polym. Degrad. Stab.* **98**(2), 527–534 (2013).
69. C. Defeyt, J. Langenbacher, and R. Rivenc, "Polyurethane coatings used in twentieth century outdoor painted sculptures. Part I: comparative study of various systems by means of ATR-FTIR spectroscopy," *Heritage Sci.* **5**(1), 11 (2017).
70. D. C. Allport and W. H. Janes, *Block Copolymers* (Applied Science Publishers, 1973).
71. C. Hepburn, *Polyurethane Elastomers*, (Elsevier Science Publishers LTD, 1992).
72. Q. Lan and G. Haugstad, "Characterization of polymer morphology in polyurethane foams using atomic force microscopy," *J. Appl. Polym. Sci.* **121**(5), 2644–2651 (2011).
73. J. H. Silver, C. W. Myers, F. Liml, and S. L. Cooper, "Effect of polyol molecular weight on the physical properties and haemocompatibility of polyurethanes containing -polyethylene oxide macroglycols," *Biomaterials* **15**(9), 695–704 (1994).